Nano Energy 74 (2020) 104749

Contents lists available at ScienceDirect

Nano Energy

journal homepage: http://www.elsevier.com/locate/nanoen

Wearable self-powered pressure sensor by integration of piezo-transmittance microporous elastomer with organic solar cell

Jungrak Choi [a], Donguk Kwon [a], Byeongsu Kim [b], Kyungnam Kang [a], Jimin Gu [a], Jihwan Jo [b], Kwangmin Na [b], Junseong Ahn [a], Dionisio Del Orbe [a], Kyuyoung Kim [a], Jaeho Park [a], Jongmin Shim [c], Jung-Yong Lee [b], Inkyu Park [a,d,*]

[a] Department of Mechanical Engineering, Korea Advanced Institute of Science and Technology (KAIST), Daejeon, 34141, South Korea
[b] Graduate School of EE (Electrical Engineering), Korea Advanced Institute of Science and Technology (KAIST), Daejeon, 34141, South Korea
[c] Department of Civil, Structural and Environmental Engineering, University at Buffalo, Buffalo, NY, 14260, USA
[d] KI for NanoCentury & Mobile Sensor and IT Convergence (MOSAIC) Center, Korea Advanced Institute of Science and Technology (KAIST), Daejeon, 34141, South Korea

ARTICLE INFO

Keywords:
Self-powered sensor
Piezo-transmittance
Microporous elastomer
Organic solar cell
Wearable sensor
Pressure sensor

ABSTRACT

There is a great demand for the development of self-powered physical sensors for wearable applications in recent years. However, it is still challenging to achieve self-powered sensors with a high stability, accuracy, and linearity. Here, a novel wearable self-powered pressure sensor based on the integration of a piezo-transmittance microporous elastomer (PTME) and a thin-film organic solar cell (OSC) is proposed. In contrast to the sensors based on other mechanisms such as piezoelectricity or triboelectricity, the proposed self-powered pressure sensor is cable of measuring static pressure continuously and stably, and utilizes the ambient light as the power source regardless of its intensity. The PTME shows the light transmittance changes by a gradual closure of micropores with compression in response to the applied pressure. This unique optical characteristics of the PTME enables the OSC to generate varying electrical current in response to the pressure. The proposed self-powered pressure sensor shows a high-performance with a sensitivity of 0.101/kPa, a linearity of $R^2 = 0.995$, and fast and reversible response to the pressure up to ~100 kPa. As practical applications of the proposed sensor, a detection of flexion/extension of a human finger for the manipulation of a prosthetic robot finger and a wind detection for the continuous monitoring of the wind speed and direction have been demonstrated.

1. Introduction

Recently, many studies on the pressure sensors with high sensitivity and flexibility have been carried out towards wearable sensor applications such as electronic skin [1–7], smart textile [8–10], flexible display [11,12], prosthetics [2], and mobile human motion sensors [4,13]. Previously, a number of piezoresistive [14–18] and capacitive [19–21] pressure sensors have been developed. However, these types of sensors require external power sources for their operations. To address this issue, numerous research for energy harvest utilizing such as piezoelectricity and triboelectricity were previously reported as self-powered sensors. For piezoelectricity-based pressure sensors, materials such as ZnO [22], lead zirconium titanate (PZT) [23], $BaTiO_3$ [24], poly (vinylidene fluoride) (PVDF) [25], and PVDF-based copolymers [26] have been employed to generate different levels of electrical power in response to dynamic pressure with high sensitivity and fast response time. In addition, triboelectricity-based pressure sensors with various combinations of materials with different triboelectric polarities and surface morphologies (e.g. micropyramids [27], micropores [28,29], nanopores/nanowires [30]) also showed successful demonstrations for detection of dynamic and repetitive pressure.

However, both the piezoelectricity-based pressure sensors and triboelectricity-based pressure sensors can only detect dynamic pressure change and lack a capability of static pressure detection due to a pulse-like voltage generation with quick decay of response [31]. Furthermore, pressure-sensing performance of both sensors have shown poor resolution with an inconsistent response to identical pressure.

In this work, to achieve high performances such as high stability, accuracy, and linearity of a self-powered pressure sensor, we propose a novel self-powered pressure sensor (piezo-transmittance based self-

* Corresponding author. Department of Mechanical Engineering, Korea Advanced Institute of Science and Technology (KAIST), Daejeon, 34141, South Korea.
E-mail address: inkyu@kaist.ac.kr (I. Park).

https://doi.org/10.1016/j.nanoen.2020.104749
Received 21 February 2020; Received in revised form 17 March 2020; Accepted 24 March 2020
Available online 11 May 2020
2211-2855/© 2020 Elsevier Ltd. All rights reserved.

powered pressure sensor; PTSPS) for wearable and portable applications by integration of microporous elastomer (PTME) with a piezo-transmittance (optical transmittance change by applying pressure) and a thin-film organic solar cell (OSC). The PTME has a property of light transmittance changes by a gradual closure of micropores with compression in response to pressure (P). A unique mechanical and optical characteristic of the PTME are employed to provide capabilities of highly sensitive and stable pressure sensing, which can cover the whole tactile pressure range (0.2–100 kPa) in a facile and cost-effective way. For the mechanical characteristics of the PTME, deformability of the PTME is regulated to induce large displacement with small pressure, enabling highly sensitive pressure response of the PTSPS. In addition, elasticity of the PTME is highly improved by minimization of visco-elastic property of a solid elastomer (SE), resulting in complete and immediate recovery of sensor responses. Regarding the optical characteristics of the PTME, the PTME shows a linear response between the relative change of current ($\Delta I/I_0$) generated by the OSC and pressure. By these characteristics, the PTSPS showed a high-performance with a sensitivity of 0.101/kPa, a linearity of $R^2 = 0.995$, and fast and reversible response for the pressure up to ~100 kPa. Finally, for practical applications, a finger motion sensor that can detect flexion/extension of a human finger for the manipulation of a prosthetic robot finger and a wind detection sensor capable of continuously monitoring wind speed and direction are demonstrated.

2. Results and discussion

A schematic design of the PTSPS is illustrated in Fig. 1. The PTSPS consists of two parts: the PTME as an active light transmission medium and the OSC as a light-induced power-generating device. To fabricate the PTME, the three-dimensional microporous elastomer was prepared by casting Ecoflex 00–30 prepolymer solutions within a sugar cube template (see Experimental Section for details). In specific, combination of a translucent (i.e. semi-transparent) characteristic of the Ecoflex 00–30 and the microporous structure could bring a great piezo-transmittance effect. For the power-generating device, the OSC has received great attention for the wearable and portable devices due to their flexibility and light weight. We employed organic solar cells using [[2,6′-4,8-di(5-ethylhexylthienyl)benzo[1,2-b;3,3-b] dithiophene][3-fluoro-2[(2-ethylhexyl)carbonyl]thieno[3,4-b]thiophenediyl]] (PTB7-

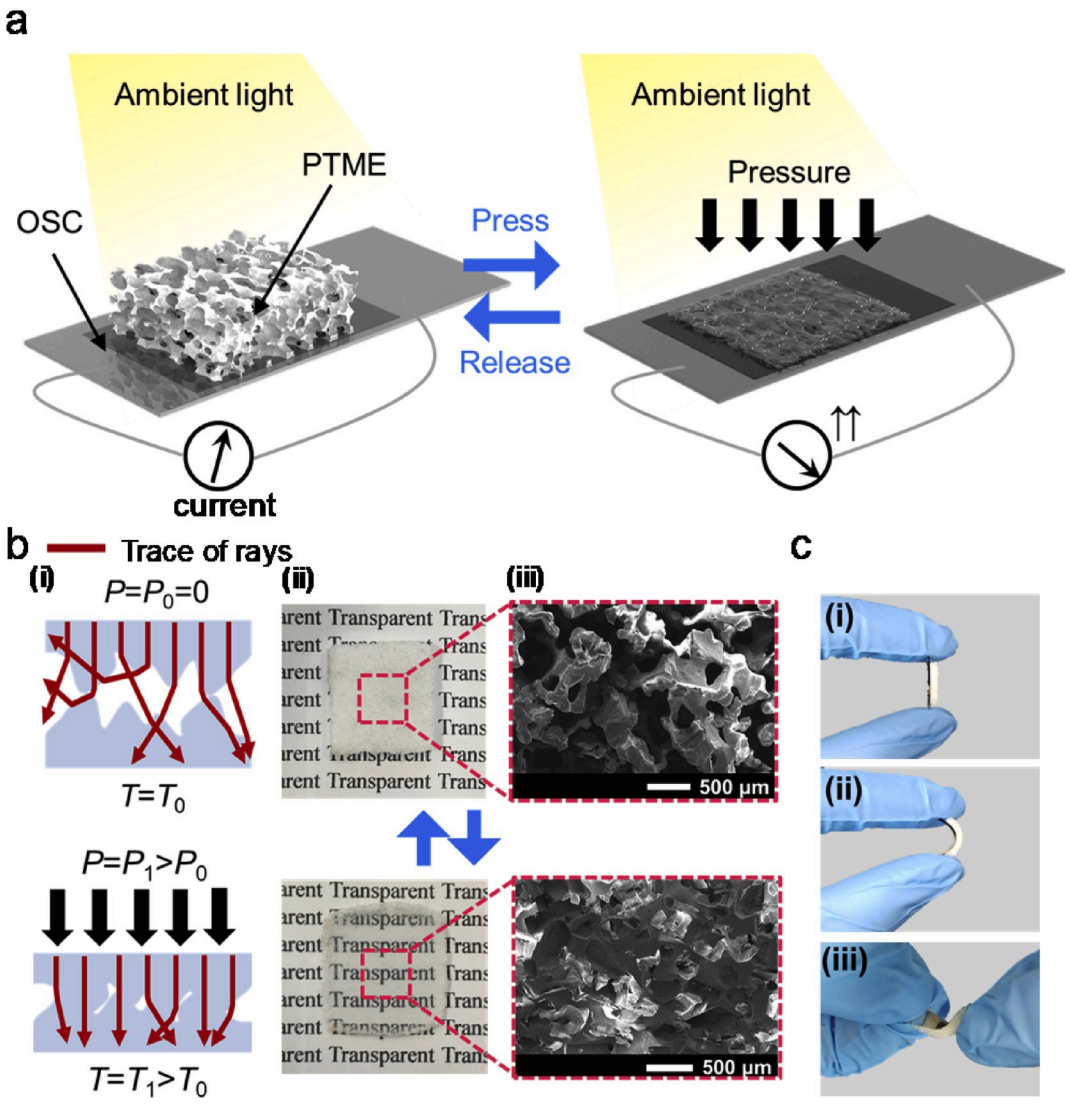


Fig. 1. Proposed piezo-transmittance based self-powered pressure sensor: (a) Schematic representation of the PTSPS. (b) Optical properties of the PTME under compression. (i) Low amount of light transmission through the PTME ($T = T_0$) due to light scattering under the uncompressed state (P=P_0=0) and higher amount of light transmission through the PTME ($T = T_1$>T_0) under the compressed state (P=P_1>P_0). (ii) Photographs of the change in transparency of the PTME before compression (top photograph) and after compression (bottom photograph). (iii) SEM images showing the pore-closing behavior of the PTME before compression (top image) and after compression (bottom image). (c) Optical images of the PTSPS showing its capability of (ii) bending and (iii) twisting.

Th) having a high sensitivity for the detection of light below indoor condition(~1 W/m^2). Besides, flexible and lightweight characteristics of the OSC is highly favorable for wearable and portable applications. Under compression, the PTME is gradually compressed with closure of micropores within its whole volume, and this allows larger quantity of light to pass through the compressed PTME than the initial state due to less scattering, leading to an increase in electrical current generated by the OSC. Therefore, the PTSPS is operated by reading the generated electrical current from the OSC beneath the PTME. The schematic illustration describing the ray traces, which pass through the uncompressed PTME and compressed PTME by applied pressure, is shown in Fig. 1b(i) In the initial state (P=P_0=0), most of light entering the PTME is scattered by the micropores randomly distributed within the whole volume of the PTME. Thus, only small amount of light is transmitted to the OSC through the PTME with a transmittance (T) value of $T = T_0$, generating low electrical current. In the compressed state (P=P_1>P_0), more micropores within the PTME get to be closed and less light scattering occurs, providing the enhanced T ($T = T_1$>T_0). Then, more light transmitted through the PTME reaches the OSC, producing higher electrical current than the case of uncompressed state. When pressure is released, the elastic resilient force of elastomer bridge fraction enables re-opening of closed micropores, and consequently the PTME recovers to its original shape, leading to the recovery of the sensor response. In Fig. 1b(ii) and Fig. 1b(iii), we can observe that the transparency and the cross-sectional morphology of the PTME in compressed and uncompressed states were characterized by transparent acrylic glass plates (see Experimental Section for details) and scanning electron microscopy (SEM). The micropores are randomly distributed within the PTME, and the micropores are closed by applied pressure as the neighboring bridges are crumpled into the micropores. The size of micropores at the initial state was observed as 400 ± 140 μm, and porosity was calculated as 72.8 ± 0.5%. In addition, the configuration of the PTME layer within its entire volume turned out to be uniform in macroscopic point of view according to the X-ray tomography image as shown in Fig. S1 and Movie S1, Supporting Information. Furthermore, from flexibility of both the PTME and the OSC, the PTSPS is capable of bending and twisting, as depicted in Fig. 1c.

Supplementary video related to this article can be found at https://doi.org/10.1016/j.nanoen.2020.104749.

In order to predict the light transmission performances of the PTME according to varying compressive strain (*CS*), we carried out a ray-tracing optical simulation. As shown in Fig. 2a, we modeled the PTME (2 mm × 2 mm × 2 mm) to describe a nonlinear constitutive compressive behavior with finite element analysis based on the Neo-Hookean hyperelastic model using the same method conducted in our previous work [32]. Then, the light paths through the PTME under different levels of compressive strain was examined to calculate the transmittance. The representative simulation results for the ray-traces transmitted through the PTME under compressive strain of 0%, 20%, 40%, 60%, and 80% are visualized to estimate the light scattering effect with respect to the compressive strain as shown in Fig. 2b. Moreover, the corresponding light intensity mappings for the distributions of transmitted light intensity at the detector can be found in Fig. S2, Supporting Information. The transmittance was calculated as a ratio of transmitted light intensity received by the detector to the incident light intensity from the surface light source. The transmittance of the PTME is gradually increased with the increase of compressive strain, showing a reasonable agreement between the experimental and simulation results as shown in Fig. 2c.

Fig. 3 displays the mechanical and optical characteristics of the PTME compared to SE with the same dimension. The compressive behaviors of the PTME and SE were investigated as shown in Fig. 3a. The compressibility was calculated as the slope of the pressure vs. compressive strain curves. The compressibility of the PTME is 6.73%/kPa (R^2 = 0.986) while that of the SE is 0.21%/kPa (R^2 = 0.991). By introducing the micropores within the PTME, the compressibility of the PTME is significantly increased by ~32 times as compared to the SE, which is critical for highly sensitive pressure sensing. For the evaluation of optical characteristics, the transmittance of the PTME over the visible light range (wavelength of 300–800 nm) under various compressive strains was measured by the ultraviolet–visible (UV–Vis) spectrophotometer as shown in Fig. 3b. The overall transmittance of the PTME in the visible light range were increased with the increase of compressive

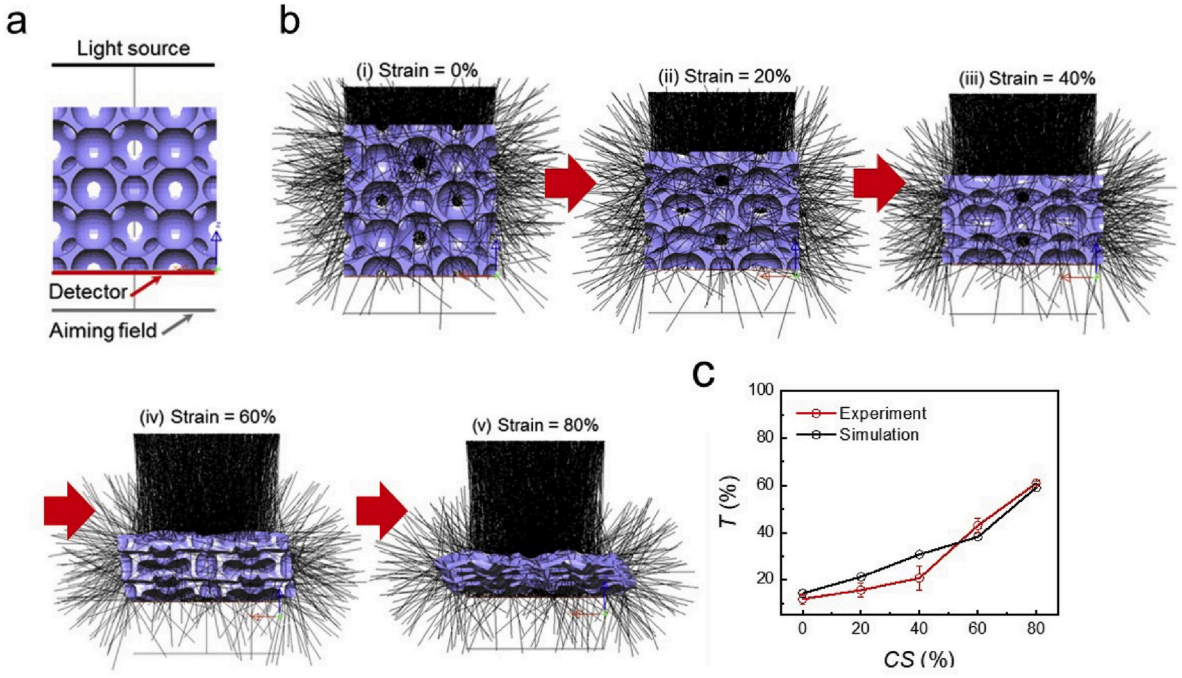


Fig. 2. Ray-tracing optical simulation results for the prediction of light transmission changes of the PTME by compressive strain: (a) Schematic illustration of the simulation model in similarity to the actual experimental set up. (b) Results of the simulation, showing the light paths transmitted through the PTME. (c) Transmittance versus compressive strain curves of the experimental data and simulation results. The transmittance of the PTME gradually increases with increasing compressive strain; the graph shows a reasonable agreement between the experimental and simulation results.

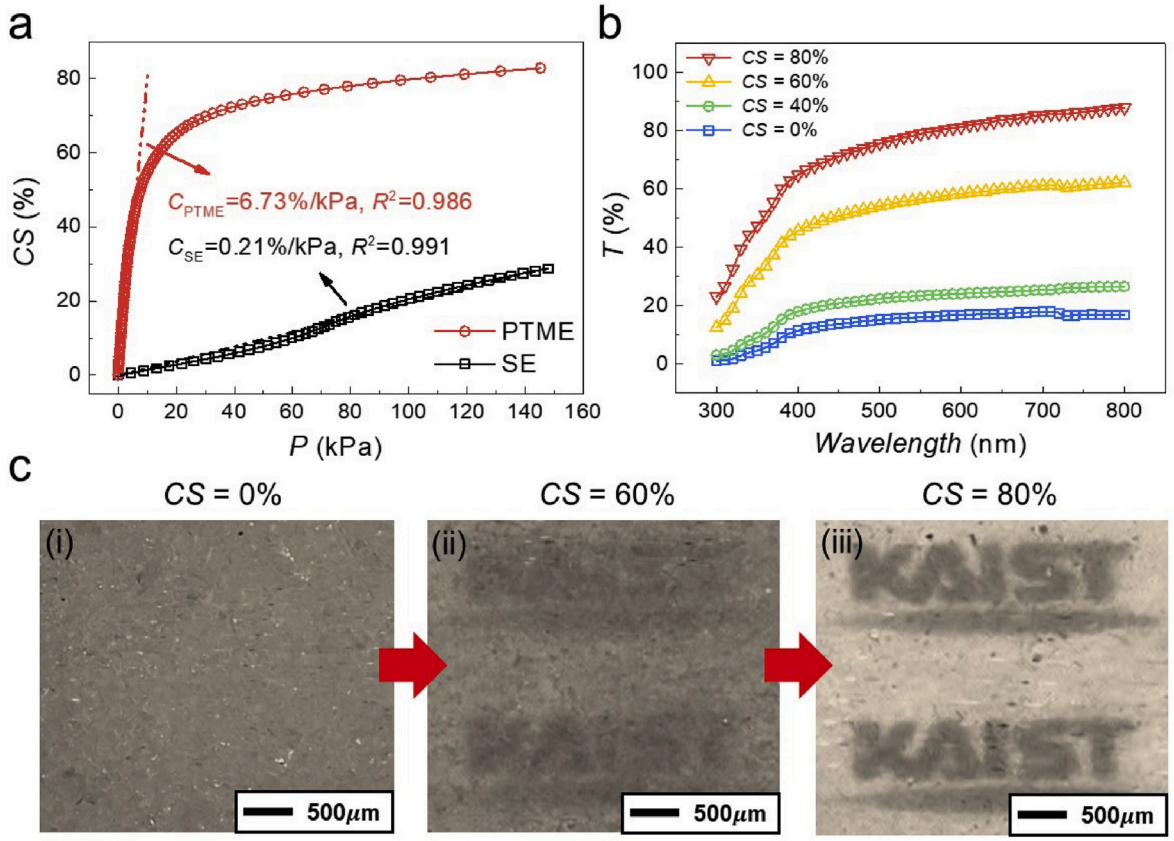


Fig. 3. Mechanical and optical characteristics of the PTME: (a) Compressive behavior of the PTME and SE. The compressibility of the PTME was 6.73%/kPa (R^2 = 0.986) while that of the SE was 0.21%/kPa (R^2 = 0.991). (b) The transmittance of the PTME over the range of visible light under various compressive strain. (c) The piezo-transmittance property of the PTME was visually captured by a CCD camera. The closure of pores occurs uniformly throughout the whole surface of the PTME, and the transparent area fraction of the PTME, which can be determined by the clarity of the institution logo (KAIST) under the PTME.

strain. To visualize the piezo-transmittance property of the PTME, the compressed PTME was captured by a charged coupled device (CCD) camera as shown in Fig. 3c (Movie S2, Supporting Information). The closure of pores occurs uniformly throughout the whole surface of the PTME and the transparency of the PTME, which can be determined by the fact that clarity of our institution logos (KAIST) under the PTME, is gradually increased with the increase of compressive strain.

Supplementary video related to this article can be found at https://doi.org/10.1016/j.nanoen.2020.104749.

Fig. 4 shows the static and dynamic pressure sensing performances of the PTSPS under incident illumination intensity of 250 W/m^2. The static pressure sensing performance was evaluated by plotting curves of the relative change of current generated by the OSC versus pressure. In Fig. 4a, the PTSPS showed highly sensitive and linear behavior with a sensitivity (defined as the slope of the curve, $S_{PTSPS} = \delta(\Delta I/I_0)/\delta P$) of 0.101/kPa up to the pressure of 150 kPa without any mechanical or electrical instability of the sensor. Its sensitivity is nearly 100 times higher than that of the SE-based self-powered pressure sensor (SESPS). Additionally, the recoverability of the PTSPS and SESPS was examined by plotting the normalized response ($\Delta P_\varepsilon/\Delta P_{\varepsilon=60\%,max}$) versus time ($t$) as shown in Fig. 4b. The step stimuli with compressive strain of 60% for 1 min were applied and each response to the step stimuli was normalized by its maximum value over the testing time. The normalized responses are indicated in Fig. 4b with the notation of $\Delta P_\varepsilon/\Delta P_{\varepsilon=60\%,max}$. While the SESPS did not show full recovery due to the viscoelastic property of the SE, the PTSPS showed a complete and immediate recovery to the original value due to the improvement of elastically resilient property. Furthermore, dynamic responses were investigated over the pressure ranges of 1–120 kPa as shown in Fig. 4c. It was observed that the PTSPS covered the tactile pressure range (1–100 kPa) with fast, stable, noise-free and perfectly reversible response. Therefore, it was confirmed that the sensitive, linear, and fully reversible pressure sensing performance is achieved by introducing the microporous configuration into the elastomeric light transmission medium. Moreover, the pressure response curves of the PTSPS under the various light intensities of 100 W/m^2, and 200 W/m^2, and 250 W/m^2 were examined as shown in Fig. 4d. From the results, it is observed that the pressure sensing performance of the PTSPS is not significantly affected by the intensity of illuminated light. In Fig. 4e, the long-term stability and electromechanical durability of the PTSPS was evaluated under 5000 cycles of repeated compression/release at ~50 kPa (compressive strain of 70%). No noticeable drift of the sensor response and no structural change of the PTME were found during the repeated compression cycles. From the results, the PTSPS is appropriate for long-term, repeated wearable applications. In Fig. 4f, the PTSPS was evaluated at different values of temperature and humidity. As temperature (T) increased from 20 to 75 °C, initial current of the PTSPS decreased. However, the relative change of current was not significantly affected. This means that the sensor can be used for practical wearable devices because most of the electrical devices for these purposes should not exceed 65 °C in general. Also, when relative humidity (RH) at 25 °C changed from 15 to 80%, no variation in the relative change of current was observed. Finally, the theoretical limit of detection (LOD) value was calculated based on the slope of linear calibration curve (a) near the LOD value and the signal-to-noise ratio (Fig. S3, Supporting Information). The noise level was estimated as 5.49×10^{-4} by a standard deviation of blank responses (σ_{blank}), which is the relative change of current by the OSC without applying pressure, and the slope of linear calibration curve near the LOD value was obtained as 0.00791/kPa. From these parameters and the equation of $LOD = 3\sigma_{blank}/a$, the theoretical LOD value was estimated as ~0.2

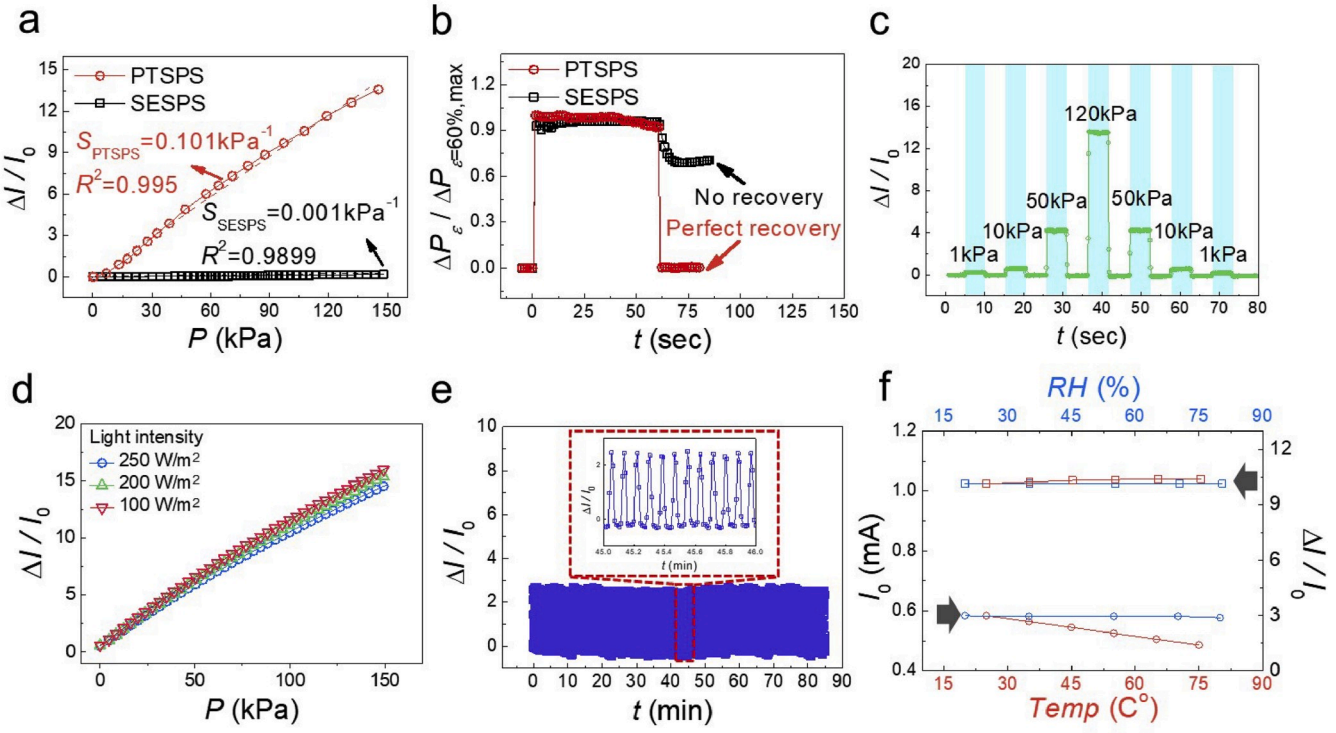


Fig. 4. Static and dynamic pressure sensing performances of the PTSPS: (a) the relative change of current versus pressure of the PTSPS compared to the SESPS. (b) Recoverability performances of the PTSPS compared to the SESPS. (c) Dynamic responses of the PTSPS to various pressure ranging from 1 kPa to 100 kPa. (d) The relative change of current versus pressure of the PTSPS under the various light intensities of 100 W/m^2, 200 W/m^2, and 250 W/m^2. (e) Long-term electromechanical stability of the PTSPS over 5000 cycles of a repeated compression/release test with a compressive strain of 70%. (f) Initial current and the relative change of current of the PTSPS under different temperature and humidity conditions.

kPa. From the result, it was verified that the *LOD* of the PTSPS is small enough to detect a subtle pressure.

For wearable devices, the dimensions of sensors are important factors for better wearability and less interference with diverse human motions and 3D shape of objects. As shown in Fig. S4, Supporting Information, the pressure-sensing performances of the PTSPS were examined for different values at $t_{thickness}$ of 1, 2, 5, and 10 mm and at $r_{bending}$ of 5, 30, and ∞ mm of the PTME (reference $t_{thickness}$ and $r_{bending}$ are 2 mm and ∞ mm, respectively). For the different thickness, the response is slightly decreased when the thickness decrease because lower thickness of the PTME has less pores in the PTME, which decrease light scattering inside of the PTME. However, this dependency is not significant for the thickness down to 2 mm. For the different bending radii, the response slightly decreased at $r_{bending}$ of 5 mm. However, the sensor over $r_{bending}$ of 30 mm showed bending-insensitive properties.

Making use of these excellent properties, we applied the PTSPS to a finger motion sensing, in which the flexion/extension of a human finger are detected and utilized for the manipulation of a prosthetic robot finger. Firstly, for the finger motion sensor, two OSCs (a sensing OSC and a reference OSC) were attached on the finger for calibrating the responses under different light intensities, i.e., To compensate the responses under different light intensities for real situations. Then, the PTME was placed only on the sensing OSC, covering the active area of the sensing OSC, and then a thin polydimethylsiloxane (PDMS) film was attached to the structure as shown in Fig. 5a. Fig. 5b shows photographic images of the sensor package and the prosthetic robot finger being controlled by using the motion sensor on the human finger. When the finger is not flexed, the PDMS film stays at its original position. When the finger is flexed, the PDMS is stretched in the horizontal direction, and it compresses the PTME in the vertical direction, which in turn changes the transmittance of the PTME. Therefore, the flexing action of the finger only changes the response of the sensing OSC when the light intensity is constant. From the response, the finger angle can be evaluated (Fig. 5c) and the prosthetic finger can be controlled to match with the human finger angle. The video for the prosthetic finger control by the finger motion sensor is shown in Movie S3, Supporting Information. However, it should be noted that the intensity of incident light can continuously change depending on the illumination conditions (i.e. different solar irradiation or indoor lighting). Therefore, we have utilized a pair of reference OSC and sensing OSC to remove this effect. In Fig. 5d, the black curve with circle markers and the blue curve with square markers represent the current generated by the reference OSC and the sensing OSC, respectively, with repeated flexion/extension motions of human finger under different light intensities. The amount of current generated by the reference OSC and the sensing OSC decreased with the decrease of light intensity. The experimental relation obtained to compensate the responses of the sensing OSC under different light intensities is shown in Fig. S5, Supporting information. Using this relationship, the calibrated relative change of current shows the desired behavior, i.e., similar response regardless of the light intensity, as shown in the red line with triangle markers. A video of the sensor responses with repeated flexion/extension motions of a human finger under different light intensities is shown in Movie S4, Supporting Information.

Supplementary video related to this article can be found at https://doi.org/10.1016/j.nanoen.2020.104749.

As another practical application of PTSPS, we demonstrated its use in the wind detection application, where the PTSPS can sense a sudden change in the wind without any supply of electricity, and it can be attached on curved surfaces, such as a turbine. Fig. 6a shows a 3D schematic depicting the components of the wind detection sensor. Here, five sensing OSCs (covered by the PTMC) and five reference OSCs were attached on the pole for detecting the wind speed and direction under different light intensities. The incoming wind compresses the PTME, placed on the sensing OSC, and based on the transmittance change

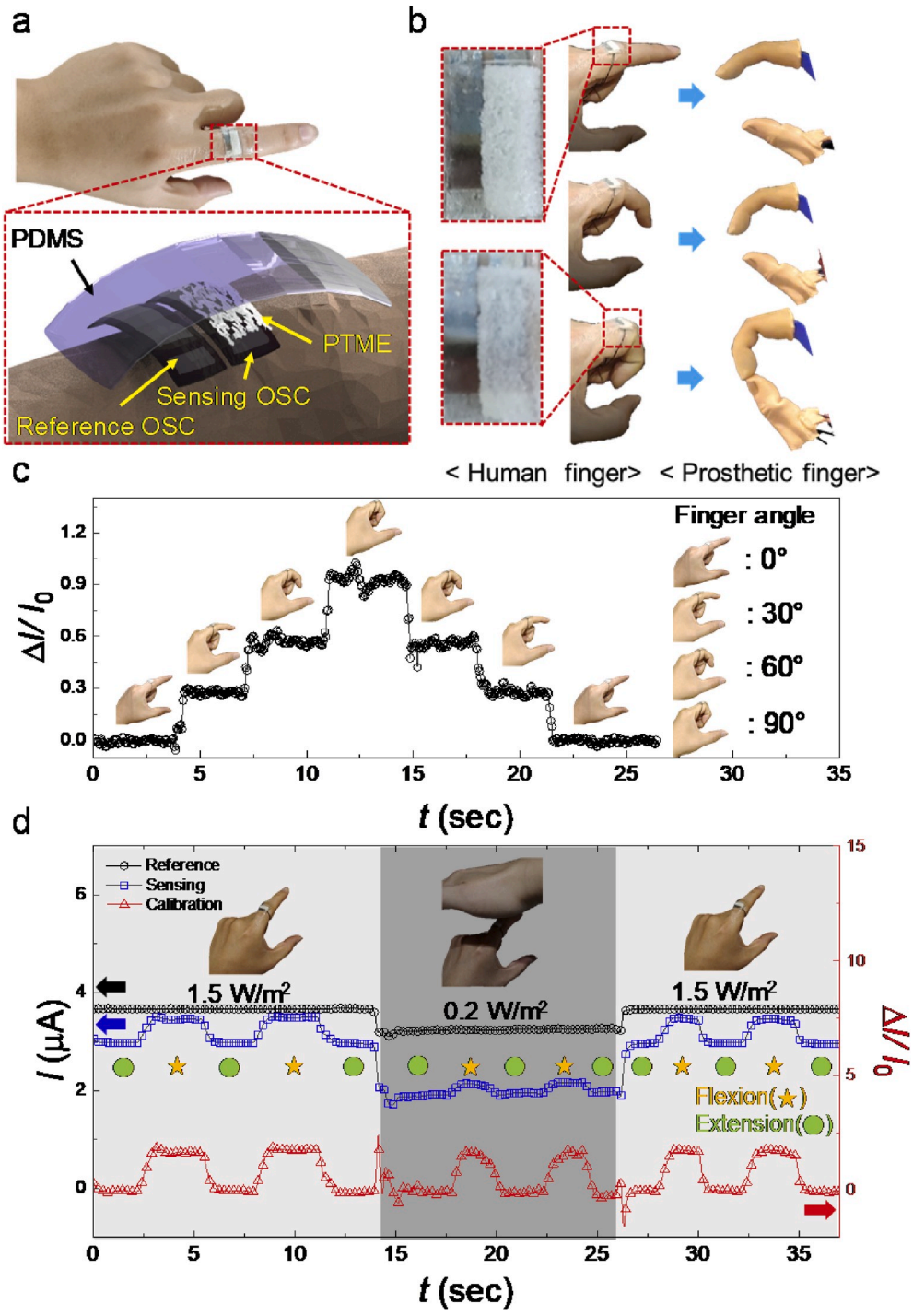


Fig. 5. Demonstration of the finger motion sensing by PTSPS for control of the prosthetic robot finger: (a) Photographic image of the finger motion sensor on the finger based on the PTME and OSC and 3D model of detailed components of the finger motion sensor. (b) Photographic images of controlling the prosthetic robot finger using the sensor on the human finger. (c) The sensor response over the finger angle of 0° – 90°. (d) The sensor responses of the sensing OSC and reference OSC and the calibrated response with repeated flexion/extension motions of human finger under different light intensities. The amount of current generated by the sensing OSC and reference OSC were decreased with the decrease of illumination intensity. However, the calibrated relative change of current shows similar tendency regardless of the light intensity as shown in the red line with a triangle marker.

induced by this compression, the speed of the wind can be estimated by the similar sensing mechanism used in the finger motion sensor. In addition, by using the array configuration shown in Fig. 6a, the direction of the wind can be determined. We used an air gun to generate the desired wind speed (4 m/s) and direction; the speed and directions were controlled by an air pressure pump and a rotatable plate, respectively. The wind speed was confirmed by a commercial anemometer. Fig. 6b shows the relative change of current on each sensor when the wind was blown continuously in the direction from S1 to S5, and then back to S1. For the enhanced visual representation of the data in Fig. 6b, a 2D color map of the signal change is plotted in polar coordinates in Fig. 6c (Fig. S6, Supporting Information). Furthermore, a demonstration video is shown in Movie S5, Supporting Information. With this, we have demonstrated the feasibility of the PTSPS for the wind detection applications with a stable, continuous and accurate detection capability.

Supplementary video related to this article can be found at https://doi.org/10.1016/j.nanoen.2020.104749.

3. Conclusion

In conclusion, we have developed a PTSPS based on a PTME, as an active light transmission medium, and a OSC, as a power generation device. The intensity of light transmitted through the PTME increases with increasing pressure due to the closure of its micropores. The light

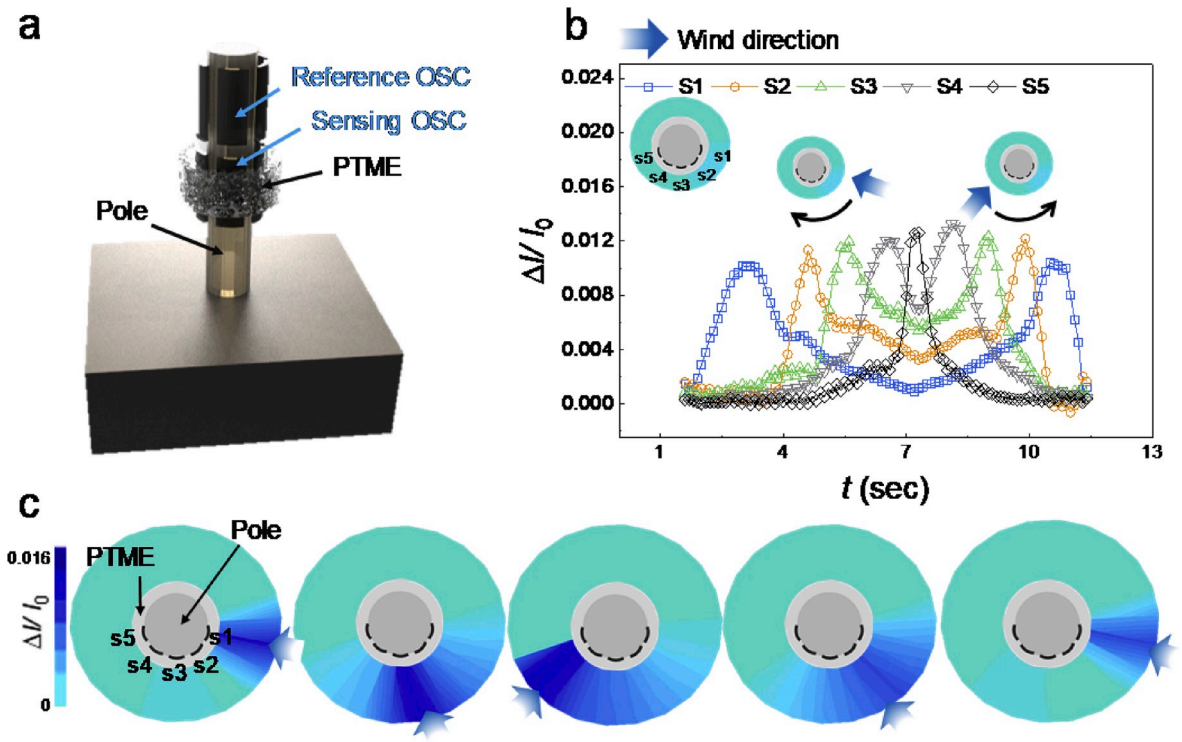


Fig. 6. Demonstration of the wind detection sensing by an array of PTSPS: (a) 3D schematic depicting the components of the wind detection sensor. The five sensing OSCs covered by the PTMC and five reference OSCs were attached on the pole for detecting the wind speed and direction under different light intensities. (b) The relative change of current on each sensor when the wind was blowing in the direction from S1 to S5 continuously and then back in the direction to S1. (c) 2D color mapping of the intensity change of each sensor in polar coordinates. The change in the signal of each sensor is represented by the darkness level of blue color.

transmitted through the PTME enters the OSC, and generates electrical current for self-powered sensing. Through ray-tracing optical simulation and experiment, it was verified that the transmittance values of the PTME are gradually increased with the increase of compression. For the sensing performance, the PTSPS showed highly sensitive and linear behavior with a sensitivity of 0.101/kPa, the linearity of $R^2 = 0.995$, and accurate, fast, and stable response over the tactile sensing range. Additionally, we confirmed the effects of light intensity, temperature, humidity, thickenss, bending radius for applying the PTSPT to practical wearable applications. From the results, we have confirmed that the PTSPS is appropriate for long-term, repeated wearable applications. Finally, we demonstrated the practical applications of PTSPS to the finger motion sensings for the human-robot interface system and wind detection sensing, without any electrical power source, and regardless of the change of external light conditions.

To the best of our knowledge, this is the first flexible self-powered pressure sensor based on the optically active structures and photovoltaic power generation devices, and as such it is expected to have a major impact on the flexible sensor industry and research in this area. Furthermore, in contrast to other sensors based on other mechanisms as piezoelectric and triboelectric sensors, our sensor is cable of measuring static pressure continuously and stably. For now, it has lower flexibility and sensitivity when compared to these other self-powered pressure sensors, such as piezoelectric and triboelectric sensors. However, this is expected to be improved with the development of new piezo-transmittance materials and more flexible organic solar cells. Therefore, we believe that our sensor, based on this novel sensing mechanism, could be an alternative solution to previous self-powered pressure sensors and applied to broader applications.

4. Experimental Section

4.1. Fabrication of PTME and SE

The PTME and SE were prepared by casting Ecoflex elastomer into a sugar cube template and a mold with the same size as the sugar cube template. The Ecoflex (Ecoflex® Shore hardness 00–30, Smooth-On, Inc., USA) prepolymer solution was poured into the sugar cube template and the mold. Then, the poured solution was degassed in a vacuum chamber. After curing at room temperature for 2 h, the sugar cube was dissolved by water to form the PTME. SE was simply detached from the mold after curing process.

4.2. Fabrication of OSC

The OSC was fabricated on the ITO deposited Polyethylene terephthalate (PET) substrate. The substrate were cleaned by sonication with detergent, acetone, isopropyl alcohol for 20 min, respectively. Next, zinc oxide (ZnO) solution using the electron transporting layer was spin coated on the substrate at 6000 rpm for 30 s. Then, this substrate was annealed at 200 °C for 20 min. For the deposition of photoactive layer, poly[4,8-bis(5-(2-ethylhexyl)thiophen-2-yl)benzo[1,2-b;4,5-b'] dithiophene-2,6-diyl-alt-(4-(2-ethylhexyl)-3-fluorothieno[3,4-b]thiophene-)-2-carboxylate-2-6-diyl)] commonly known as PTB7-Th and [6,6]-Phenyl C_{71} butyric acid methyl ester ($PC_{71}BM$) was mixed with a weight ratio of 1:1.5. Then, 20 mg of this mixture was dissolved in 1 ml of chlorobenzene with 30 μl of 1–8 diiodooctane. This solution was spin coated on the ZnO coated substrate at 2500 rpm for 30 s. After drying in a N_2 glove box for 30 min, molybdenum oxide layer with a thickness of 10 nm and silver electrode layer with a thickness of 150 nm were deposited by thermal evaporation. The fabricated OSC can be shown in Fig. S7, Supporting Information.

4.3. Characterization of PTME and SE

A high-precision universal testing machine (AGS-X, SHIMADZU, Japan) was used to evaluate the mechanical property of the PTME. A disk-type compression fixture with a diameter of 40 mm was utilized for uniform deformation of the PTME. A position-controlled compression test was conducted at a compressive speed of 0.05 mm/s. The cross-sectional morphologies of the PTME were characterized by field emission scanning electron microscopy (FE-SEM, Sirion, FEI, USA). The internal structure of the PTME was nondestructively visualized by high-resolution micro computed tomography (Micro-CT, SkyScan 1272, Bruker AXS, USA). For the optical characteristics, firstly, a CCD camera was used to visualized the piezo-transmittance property of the PTME (Fig. S8, Supporting Information). Secondly, a ray-tracing optical simulation (Light Tools®, USA), a solar illuminator (LAX-C100 Xenon light source, Asahi Spectra Co., Ltd., Inc., Japan), and a photodiode power sensor (S120C, Thorlabs, Inc., USA) with a USB power and energy interface (PM100USB, Thorlabs, Inc., USA) were used to predict the light transmission performances. As a light source to characterize the sensor performance, the solar illuminator with a range ($\lambda = 400–800$ nm) was employed (Fig. S9, Supporting Information). Regarding the actual experimental conditions, the illuminator was located at 0.5 mm above the top surface of the PTME and the photodiode power sensor was located below the PTME. The simulation conditions were set as same as the actual experimental conditions. Third, the optical transmittance of the PTME was measured by UV-VIS spectrophotometer (Lambda 1050, Perkin Elmer, USA).

4.4. Characterization of PTSPS and SESPS

To measure the static and dynamic response of the sensor, a linear stage (SAS, SAMICK THK, Korea) and a load cell (SM-500 N, Interface, USA) were used under displacement control with a source meter (Keithley 2400, Tektronix, USA) and solar illuminator (LAX-C100 Xenon light source, Asahi Spectra Co., Ltd., Inc., Japan) with collimator as shown in Fig. S10, Supporting Information. Temperature and humidity were monitored using an IR camera (E30, FLIR, USA) and a humidity sensor (SHT31 SMART, Sensiron, USA), respectively.

4.5. Demonstration of finger motion sensor for control of prosthetic robot finger and wind detection sensor

For wearable application, output from the OTSCs were measured by an Arduino Uno and a 16-bit resolution ADC (ADS1115, Adafruit, USA) with an Op-amp (MCP6004, MICROCHIP, USA) circuit (Fig. S11, Supporting Information). Then, using MATLAB (MATLAB 2018, Mathworks Inc., USA), the raw data was plotted. For the finger motion sensor, two OSC (sensing OSC, reference OSC) were attached on the finger. Then, the PTME was placed only on the sensing OSC, covering the active area of the sensing OSC, and then a thin polydimethylsiloxane (PDMS) film was attached to the structure. A prosthetic robot finger was fabricated by first building its skeleton and then covering it with a thin skin-like elastomer. For the first part, a human hand was scanned by a 3D scanner (XYZ Printing, Taiwan) for modeling the skeleton of the robot fingers. After that, the skeleton of the robot fingers was printed by a 3D printer using thermoplastic polyurethane. The robot finger was then connected to a servo motor (DM-S0300D, China) with threads for its actuation. For the second part, thin skin-like elastomer was fabricated by the following three sequential steps. First, Alja Safe powder (Smooth-On, USA) was mixed with water to form a rubbery elastomer, which was subsequently poured into a container. Second, human fingers were dipped into the container for 5 min until it was cured to form a mold for the skin-like elastomer. Finally, Ecoflex00-35 prepolymers (Smooth-On, USA) were poured into the mold back and forth to form a thin skin-like film conformably around the mold (Fig. S12, Supporting Information). When the finger is flexed, the PDMS is stretched in the horizontal direction, and it compresses the PTME in the vertical direction, which in turn changes the transmittance of the PTME. Therefore, the microcontroller in Arduino can measure the current generated by two OSCs using the Op-amp and the ADC circuit as shown in Fig. S11. At the same time, the microcontroller send the signal to the servo motor to flex the prosthetic finger based on the current generated by two OSCs. For the wind detection sensor, the five sensing OSCs covered by the PTMC and five reference OSCs were attached on the 3D printed pole ($r = 5$ mm). For an air generation system, we used an air gun (Denkousyounendan, Japan) to make artificial windy condition experimentally. The wind speed and direction were controlled by an air pressure pump (Denkousyounendan, Japan) and a rotatable plate. Also, the wind speed was confirmed by a commercial anemometer (Testo, 450i, Germany).

Declaration of competing interest

The authors declare that they have no known competing financial interests or personal relationships that could have appeared to influence the work reported in this paper.

CRediT authorship contribution statement

Jungrak Choi: Writing - original draft, Writing - review & editing, Investigation, Formal analysis, Methodology, Visualization, Conceptualization. **Donguk Kwon:** Writing - original draft, Writing - review & editing, Investigation, Formal analysis, Methodology, Conceptualization. **Byeongsu Kim:** Writing - review & editing, Methodology. **Kyungnam Kang:** Formal analysis, Methodology, Resources. **Jimin Gu:** Formal analysis, Methodology. **Jihwan Jo:** Formal analysis, Methodology, Resources. **Kwangmin Na:** Writing - review & editing, Methodology. **Junseong Ahn:** Formal analysis, Methodology. **Dionisio Del Orbe:** Writing - review & editing. **Kyuyoung Kim:** Formal analysis, Methodology. **Jaeho Park:** Formal analysis, Methodology. **Jongmin Shim:** Software, Validation, Formal analysis, Methodology. **Jung-Yong Lee:** Writing - review & editing, Methodology, Conceptualization. **Inkyu Park:** Supervision, Project administration, Writing - review & editing, Formal analysis, Methodology, Conceptualization.

Acknowledgements

J. Choi and D. Kwon contributed equally to this work. This work was supported by the following research grants: (1) This work was supported by the National Research Foundation of Korea (NRF) grant funded by the Korea government (MSIT) (No. 2018R1A2B2004910). and (2) This work was supported by the National Research Foundation of Korea (NRF) Grant funded by the Korean Government (MSIP) (No. 2015R1A5A1037668).

Appendix A. Supplementary data

Supplementary data to this article can be found online at https://doi.org/10.1016/j.nanoen.2020.104749.

References

[1] C. Wang, D. Hwang, Z. Yu, K. Takei, J. Park, T. Chen, B. Ma, A. Javey, User-interactive electronic skin for instantaneous pressure visualization, Nat. Mater. (2013) 899–904.
[2] J. Kim, M. Lee, H.J. Shim, R. Ghaffari, H.R. Cho, D. Son, Y.H. Jung, M. Soh, C. Choi, S. Jung, K. Chu, D. Jeon, S.T. Lee, J.H. Kim, S.H. Choi, T. Hyeon, D.H. Kim, Stretchable silicon nanoribbon electronics for skin prosthesis, Nat. Commun. (2014) 1–11.
[3] S. Yun, S. Park, B. Park, Y. Kim, S.K. Park, S. Nam, K.U. Kyung, Polymer-waveguide-based flexible tactile sensor array for dynamic response, Adv. Mater. (2014) 4474–4480.
[4] Z. Wu, W. Ding, Y. Dai, K. Dong, C. Wu, L. Zhang, Z. Lin, J. Cheng, Z.L. Wang, Self-Powered multifunctional motion sensor enabled by magnetic-regulated triboelectric nanogenerator, ACS Nano (2018) 5726–5733.

[5] L. Zhang, Y. Fu, L. Xing, B. Liu, Y. Zhang, X. Xue, A self-powered flexible vision electronic-skin for image recognition based on a pixel-addressable matrix of piezophototronic ZnO nanowire arrays, J. Mater. Chem. C. (2017) 6005–6013.
[6] Y. Dai, Y. Fu, H. Zeng, L. Xing, Y. Zhang, Y. Zhan, X. Xue, A self-powered brain-linked vision electronic-skin based on triboelectric-photodetecing pixel-addressable matrix for visual-image recognition and behavior intervention, Adv. Funct. Mater. (2018) 1800275.
[7] Y. Fu, M. Zhang, Y. Dai, H. Zeng, C. Sun, Y. Han, L. Xing, S. Wang, X. Xue, Y. Zhan, Y. Zhang, A self-powered brain multi-perception receptor for sensory-substitution application, Nanomater. Energy (2018) 43–52.
[8] L.M. Castano, A.B. Flatau, Smart fabric sensors and e-textile technologies: a review, Smart Mater. Struct. (2014) 53001.
[9] M. Stoppa, A. Chiolerio, Wearable electronics and smart textiles: a critical review, Sensors (2014) 11957–11992.
[10] E. Torres Alonso, D.P. Rodrigues, M. Khetani, D.-W. Shin, A. De Sanctis, H. Joulie, I. de Schrijver, A. Baldycheva, H. Alves, A.I.S. Neves, S. Russo, M.F. Craciun, Graphene electronic fibres with touch-sensing and light-emitting functionalities for smart textiles, Npj Flex. Electron. (2018) 1–6.
[11] J.H. Koo, D.C. Kim, H.J. Shim, T.H. Kim, D.H. Kim, Flexible and stretchable smart display: materials, fabrication, device design, and system integration, Adv. Funct. Mater. (2018) 1801834.
[12] J. Sheng, H.J. Jeong, K.L. Han, T.H. Hong, J.S. Park, Review of recent advances in flexible oxide semiconductor thin-film transistors, J. Infect. Dis. (2017) 159–172.
[13] L. Tai, G. Paolo, M. Liu, Virtual-to-real deep reinforcement learning: continuous control of mobile robots for mapless navigation, in: IEEE Int. Conf. Intell. Robot. Syst., 2017, pp. 31–36.
[14] K. Kim, J. Park, J. hoon Suh, M. Kim, Y. Jeong, I. Park, 3D printing of multiaxial force sensors using carbon nanotube (CNT)/thermoplastic polyurethane (TPU) filaments, Sensors Actuators, A Phys. (2017) 493–500.
[15] H. Lee, D. Kwon, H. Cho, I. Park, J. Kim, Soft nanocomposite based multi-point, multi-directional strain mapping sensor using anisotropic electrical impedance tomography, Sci. Rep. (2017) 1–10.
[16] J. Lee, H. Kwon, J. Seo, S. Shin, J.H. Koo, C. Pang, S. Son, J.H. Kim, Y.H. Jang, D. E. Kim, T. Lee, Conductive fiber-based ultrasensitive textile pressure sensor for wearable electronics, Adv. Mater. (2015) 2433–2439.
[17] K. Park, S. Kim, H. Lee, I. Park, J. Kim, Low-hysteresis and low-interference soft tactile sensor using a conductive coated porous elastomer and a structure for interference reduction, Sensors Actuators, A Phys. (2019) 541–550.
[18] Y. Pang, K. Zhang, Z. Yang, S. Jiang, Z. Ju, Y. Li, X. Wang, D. Wang, M. Jian, Y. Zhang, R. Liang, H. Tian, Y. Yang, T.L. Ren, Epidermis microstructure inspired graphene pressure sensor with random distributed spinosum for high sensitivity and large linearity, ACS Nano (2018) 2346–2354.
[19] J.O. Kim, S.Y. Kwon, Y. Kim, H.B. Choi, J.C. Yang, J. Oh, H.S. Lee, J.Y. Sim, S. Ryu, S. Park, Highly ordered 3D microstructure-based electronic skin capable of differentiating pressure, temperature, and proximity, ACS Appl. Mater. Interfaces (2019) 1503–1511.
[20] S.H. Cho, S.W. Lee, S. Yu, H. Kim, S. Chang, D. Kang, I. Hwang, H.S. Kang, B. Jeong, E.H. Kim, S.M. Cho, K.L. Kim, H. Lee, W. Shim, C. Park, Micropatterned pyramidal ionic gels for sensing broad-range pressures with high sensitivity, ACS Appl. Mater. Interfaces (2017) 10128–10135.
[21] L. Viry, A. Levi, M. Totaro, A. Mondini, V. Mattoli, B. Mazzolai, L. Beccai, Flexible three-axial force sensor for soft and highly sensitive artificial touch, Adv. Mater. (2014) 2659–2664.
[22] S. Liu, L. Wang, X. Feng, Z. Wang, Q. Xu, S. Bai, Y. Qin, Z.L. Wang, Ultrasensitive 2D ZnO piezotronic transistor array for high resolution tactile imaging, Adv. Mater. (2017) 1606346.
[23] S. Xu, B.J. Hansen, Z.L. Wang, Piezoelectric-nanowire-enabled power source for driving wireless microelectronics, Nat. Commun. (2010) 1–5.
[24] S.M. Villa, V.M. Mazzola, T. Santaniello, E. Locatelli, M. Maturi, L. Migliorini, I. Monaco, C. Lenardi, M. Comes Franchini, P. Milani, Soft piezoionic/piezoelectric nanocomposites based on ionogel/BaTiO 3 nanoparticles for low frequency and directional discriminative pressure sensing, ACS Macro Lett. (2019) 414–420.
[25] M. Bobinger, S. Keddis, S. Hinterleuthner, M. Becherer, F. Kluge, N. Schwesinger, J. F. Salmeron, P. Lugli, A. Rivadeneyra, Light and pressure sensors based on PVDF with sprayed and transparent electrodes for self-powered wireless sensor nodes, IEEE Sensor. J. (2019) 1114–1126.
[26] S. Kim, I. Towfeeq, Y. Dong, S. Gorman, A.M. Rao, G. Koley, P.(Vdf-TrFE, Film on PDMS substrate for energy harvesting applications, Appl. Sci. (2018) 213.
[27] C.L. Choong, M.B. Shim, B.S. Lee, S. Jeon, D.S. Ko, T.H. Kang, J. Bae, S.H. Lee, K. E. Byun, J. Im, Y.J. Jeong, C.E. Park, J.J. Park, U.I. Chung, Highly stretchable resistive pressure sensors using a conductive elastomeric composite on a micropyramid array, Adv. Mater. (2014) 3451–3458.
[28] O. Atalay, A. Atalay, J. Gafford, C. Walsh, A highly sensitive capacitive-based soft pressure sensor based on a conductive fabric and a microporous dielectric layer, Adv. Mater. Technol. (2018) 1700237.
[29] W. Deng, X. Huang, W. Chu, Y. Chen, L. Mao, Q. Tang, W. Yang, Microstructure-Based interfacial tuning mechanism of capacitive pressure sensors for electronic skin, J. Sensors. (2016) 8.
[30] S. Yao, Y. Zhu, Wearable multifunctional sensors using printed stretchable conductors made of silver nanowires, Nanoscale (2014) 2345–2352.
[31] J. Rao, Z. Chen, D. Zhao, Y. Yin, X. Wang, F. Yi, Recent Progress in Self-Powered Skin Sensors, 2019, pp. 1–19.
[32] D. Kwon, T.I. Lee, J. Shim, S. Ryu, M.S. Kim, S. Kim, T.S. Kim, I. Park, Highly sensitive, flexible, and wearable pressure sensor based on a giant piezocapacitive effect of three-dimensional microporous elastomeric dielectric layer, ACS Appl. Mater. Interfaces (2016) 16922–16931.



Jungrak Choi is currently a Ph.D candidate at the Korea Advanced Institute of Science and Technology (KAIST). he received her M.S. degree at KAIST and DTU in 2018. His current research interest is focused on the soft material based sensors and stretchable electronics for healthcare application.



Donguk Kwon is currently a staff engineer at Samsung Electronics. In 2018, he received a Ph.D. in mechanical engineering from KAIST. His current research interest is the development of an advanced packaging process.



Byeongsu Kim is currently Ph.D. student under the guidance of Prof. Jung-Yong Lee in the key laboratory of novel thin film solar cells, Korea Advanced Institute of Science and Technology. His current research interest is organic-quantum dot hybrid solar cells.



Kyungnam Kang is currently an Engineer at the Samsung Electronics. He received his Ph.D. degree at KAIST in 2019. His current research interest is focused on the highly integrated and low power gas sensor system for IoT(Internet of things) applications.



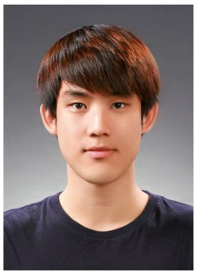
Jimin Gu is currently a Ph.D candidate at the Korea Advanced Institute of Science and Technology (KAIST). She received her M.S. degree at KAIST in 2019. Her current research interest is focused on the soft material based sensors and stretchable electronics for biomedical and healthcare application.



Jiwhan Jo is currently Ph.D student under the guidance of Prof. Jung-Yong Lee in Korea Advanced Institute of Science and Technology. His current research interest is nanomorphology control in organic solar cell.



Kwangmin Na currently works on Korea electric power corporation (KEPCO). He received M.S. degree under the guidance of Prof. Jung-Yong Lee in Korea Advanced Institute of Science and Technology.



Junseong Ahn is currently a Ph.D. student at the Korea Advanced Institute of Science and Technology (KAIST). He received his M.S. degree at KAIST in 2019. His current research interest is focused on the micro/nano structuring.



Dionisio Del Orbe received his Bachelor's degree from Western Michigan University in 2012 and Master's degree from Rochester Institute of Technology in 2015. Currently, he is a PhD student in Prof. Inkyu Park's Micro and Nano Transducer (MINT) Laboratory in KAIST. His research interests include flexible physical sensors and chemical gas sensors.



Kyuyoung Kim is Ph.D. candidate in department of mechanical engineering, Korea Advanced Institute of Science and Technology. His research interests are development of wearable soft sensors and their applications on health monitoring and smart electronic-skin.



Jaeho Park is currently a post-doctoral researcher at the Korea Advanced Institute of Science and Technology (KAIST). He received his Ph.D. degree at KAIST in 2019. His current research interest is focused on the microscale biosensor and the sensor-integrated system toward biomedical applications.



Jongmin Shim is an Associate Professor in the Department of Civil, Structural, and Environmental Engineering at the University at Buffalo. He received his Ph.D. in Engineering Mechanics at MIT. He is interested in applying elastic instability to the design of mechanical metamaterials. For the last few years, he has been identifying the underlying mechanisms of instability-induced pattern transformations and their applications to tunable phononic crystals, soft reconfigurable structures, and encapsulation structures, and dynamic façades.



Jung-Yong Lee is a professor in the school of Electrical Engineering at Korea Advanced Institute of Science and Technology (KAIST), and currently leads the Advanced Devices for Energy Conversion (ADEC) laboratory. He received his Ph.D. degree in Electrical Engineering at Stanford University. He has discovered novel solution processing method named spontaneous spreading. His present interests include organic, quantum dot and perovskite based optoelectronic devices and related transparent conducting electrodes.



Inkyu Park received his B.S., M.S., and Ph.D. from KAIST (1998), UIUC (2003) and UC Berkeley (2007), respectively, all in mechanical engineering. He has been with the department of mechanical engineering at KAIST since 2009 as a faculty and is currently a KAIST Chair Professor. His research interests are nanofabrication, smart sensors, nanomaterial-based sensors and flexible & wearable electronics. He has published more than 100 international journal articles (SCI indexed) and 130 international conference proceeding papers in the area of MEMS/NANO engineering. He is a recipient of IEEE NANO Best Paper Award (2010) and HP Open Innovation Research Award (2009–2012).